Vertical dispersion of Lagrangian tracers in fully developed stably stratified turbulence

N. E. Sujovolsky and P. D. Mininni
Departamento de Física, Facultad de Ciencias Exactas y Naturales, Universidad de Buenos Aires, 1428 Buenos Aires, Argentina
and IFIBA, CONICET, Ciudad Universitaria, 1428 Buenos Aires, Argentina

(Received 12 September 2018; published 29 January 2019)

We study the effect of different forcing functions and of the local gradient Richardson number Ri_g on the vertical transport of Lagrangian tracers in stably stratified turbulence under the Boussinesq approximation and present a wave and continuous-time random-walk model for single- and two-particle vertical dispersion. The model consists of a random superposition of linear waves with their amplitude, based on the observed Lagrangian spectrum of vertical velocity, and a random-walk process to capture overturning that depends on the statistics of Ri_g among other Eulerian quantities. The model is in good agreement with direct numerical simulations of stratified turbulence, where single- and two-particle dispersion differ from the homogeneous and isotropic case. Moreover, the model gives insight into the mixture of linear and nonlinear physics in the problem, as well as on the different processes responsible for vertical turbulent dispersion.

DOI: 10.1103/PhysRevFluids.4.014503

I. INTRODUCTION

Stably stratified turbulence (SST) is common in geophysical flows, as the ocean and the atmosphere are usually in a turbulent state and affected by stratification (and rotation at the largest scales), making it of fundamental importance in the study of dispersion of pollutants, transport of nutrients, and turbulent mixing in a wide range of scales [1–4]. As stably stratified turbulence is anisotropic, it is also inherently different from homogeneous isotropic turbulence (HIT) [5–8]. In SST, the stratification reduces the vertical velocity, confining the flow into a quasihorizontal layered motion and generating vertically sheared horizontal winds (VSHWs) with high vertical variability [9]. The stratification also results in a restoring force, allowing for the excitation of waves that can coexist with the turbulence.

As a result, vertical and horizontal turbulent transports in SST are fundamentally different. It has been speculated that horizontal transport could be more efficient than in HIT due to the presence of VSHWs [9,10]. Indeed, horizontal dispersion is dominated by the VSHWs, as shown in direct numerical simulations and by our recent model for horizontal particle dispersion in Ref. [11]. This study also showed that the characteristic timescales of dispersion in the vertical and horizontal directions are very different. This difference is used in the present work to study vertical dispersion separately from its horizontal counterpart. For vertical transport and dispersion, stratification has some obvious and some not-so-obvious implications [12–14]. On the one hand, the vertical velocity in SST is intermittent, implying that arguments based solely on mean values of the vertical velocity or its power spectrum could be misleading due to the spontaneous occurrence of extreme values [15,16]. On the other hand, while it is well understood that in stratified turbulence as the stratification is increased the mean vertical velocity is quenched, vertical gradients also increase with increasing stratification, possibly balancing the vertical transport [5,17,18].

Mixing in stratified turbulence has been largely studied from an Eulerian point of view [19–24], but Lagrangian measurements with floaters are also common nowadays, especially in

oceanic measurements of waves and turbulence [2], where they are relevant to understand the transport of nutrients with applications for the fishing industry. Vertical dispersion is also important in the atmosphere [25] and particle dispersion has also been studied recently in atmospheric flows for forecasting purposes using Lagrangian models [26]. In spite of this, there are few studies of stratified turbulence from the Lagrangian point of view [27–29], where linear theories of SST predict the bounding of particles in vertical layers and the saturation for long times of single- and two-particle vertical dispersion [28]. However, these linear models cannot capture the effect of overturning, or of thermal diffusion, which can be relevant at intermediate times and dominate the dynamics of the vertical transport at very long times [29]. It is also worth noting that inertial particles with density different from that of the fluid are also relevant to study transport and have received substantial attention in HIT (see, e.g., [30,31]), with special emphasis on the mechanisms leading to its spatial distribution and clustering. However, transport and distribution of inertial particles in SST have also been studied only recently [4,32–34].

In this paper we present several direct numerical simulations (DNSs) of the Boussinesq equations with Reynolds buoyancy numbers $\mathrm{Rb} > 1$ in two different domains, one cubic and the other anisotropic (an elongated domain with the horizontal sides longer than the vertical), and using two different mechanical forcing functions. We applied random forcing (RND) or a Taylor-Green forcing (TG), which generates a coherent large-scale flow at the largest available scales, thus affecting vertical transport. The Boussinesq Eulerian flow is evolved together with Lagrangian particles. We study single- and two-particle vertical dispersion and analyze the role of the Froude number, the vertical shear, the large-scale flow, and the local gradient Richardson number in the vertical dispersion of particles. We also present a model for single- and two-particle vertical dispersion that is in good agreement with the DNS results. In a previous work [11], we focused on the study of horizontal displacements of Lagrangian particles in SST and we developed a model for single-particle horizontal dispersion; single-particle vertical displacements were considered, but at moderate values of Rb and in cases dominated by waves. The model introduced here for vertical dispersion, together with the results in Ref. [11] for horizontal dispersion, provides a description of transport of Lagrangian tracers in SST in both the horizontal and vertical directions, for a wide range of parameters, and for both early and late times in the particles' evolution. In particular, the superposition of linear and turbulent effects in the model for vertical dispersion presented in this work allows us to identify the leading physical effects resulting in vertical dispersion at early and at late times (compared with the period of the internal gravity waves). Moreover, as all parameters in the model can be obtained from large-scale Eulerian data, the model could be used autonomously to obtain statistical predictions of vertical particle dispersion provided a large-scale flow.

II. NUMERICAL SIMULATIONS

For this study we solved numerically the incompressible Boussinesq equations for the velocity $\mathbf{u}$ and for buoyancy (or temperature) fluctuations θ,

$$\partial_t \mathbf{u} + \mathbf{u}\cdot\boldsymbol{\nabla}\mathbf{u} = -\boldsymbol{\nabla} p - N\theta\hat{z} + \nu\nabla^2\mathbf{u} + \mathbf{f}, \tag{1}$$

$$\partial_t \theta + \mathbf{u}\cdot\boldsymbol{\nabla}\theta = N\mathbf{u}\cdot\hat{z} + \kappa\nabla^2\theta, \tag{2}$$

$$\boldsymbol{\nabla}\cdot\mathbf{u} = 0, \tag{3}$$

where p is the correction to the hydrostatic pressure, ν is the kinematic viscosity, $\mathbf{f}$ is an external mechanical forcing, N is the Brunt-Väisälä frequency (which sets the stratification), and κ is the diffusivity. In terms of the density fluctuations ρ, the Brunt-Väisälä frequency is $N^2 = -(g/\rho_0)(d\bar{\rho}/dz)$, with $d\bar{\rho}/dz$ the imposed (linear) background density stratification and ρ_0 the mean density. We write the buoyancy field θ in units of velocity by defining $\theta = g\rho/\rho_0 N$. All quantities are then made dimensionless using a characteristic length L_0 and a characteristic velocity U_0. All runs in this paper have a Prandtl number $\mathrm{Pr} = \nu/\kappa = 1$.

The Boussinesq equations were solved in a three-dimensional periodic domain, using a parallelized and fully dealiased pseudospectral method and a second-order Runge-Kutta scheme for time integration [35]. In the turbulent steady state of each simulation we also injected $O(10^6)$ Lagrangian particles and integrated their trajectories in time using

$$\mathbf{v}_i = \frac{d\mathbf{x}_i}{dt} = \mathbf{u}(\mathbf{x}_i, t), \tag{4}$$

where the subindex i labels each particle. Here and in the following, the velocity of Lagrangian particles and its Cartesian components are represented as $\mathbf{v} = (v_x, v_y, v_z)$, while the Eulerian fluid velocity is given by $\mathbf{u} = (u_x, u_y, u_z)$. Integration of particles' trajectories was done using a second-order Runge-Kutta method in time and a three-dimensional cubic spline spatial interpolation to estimate Lagrangian velocities at the particles positions $\mathbf{x}_i$ from the velocity $\mathbf{u}$ in the regular Eulerian grid [36]. All simulations were done using the GHOST code (geophysical high-order suite for turbulence), recently extended to work with noncubic boxes [37].

Equations (1) and (2) have two controlling dimensionless parameters, the Reynolds and the Froude numbers, respectively, given by

$$\mathrm{Re} = \frac{LU}{\nu}, \quad \mathrm{Fr} = \frac{U}{LN}, \tag{5}$$

where L and U are, respectively, the characteristic Eulerian integral length and rms velocity of the flow. From Eq. (5) we can also define the buoyancy Reynolds number

$$\mathrm{Rb} = \mathrm{Re}\,\mathrm{Fr}^2, \tag{6}$$

which gives an estimation of how turbulent the flow is at the buoyancy scale $L_b = U/N$ and as a result can be expected to play an important role in turbulent transport. In the following we will consider simulations with $\mathrm{Rb} > 1$. The Ozmidov scale $L_{\mathrm{Oz}} = 2\pi/k_{\mathrm{Oz}}$ (with $k_{\mathrm{Oz}} = \sqrt{N^3/\epsilon}$ and ϵ the energy injection rate) will also play an important role in the following discussion, as for scales sufficiently small when compared with L_{Oz} the flow is expected to recover isotropy. When $\mathrm{Rb} > 1$ the Ozmidov scale is larger than the Kolmogorov dissipation scale η and quasi-isotropic turbulent transport can thus be expected to take place at small scales. Another parameter that will be useful to quantify small-scale turbulence and transport is the local gradient Richardson number

$$\mathrm{Ri}_g = \frac{N(N - \partial_z\theta)}{(\partial_z u_\perp)^2}, \tag{7}$$

where $u_\perp$ is the horizontal velocity. When $\mathrm{Ri}_g < 1/4$ the flow can develop shear instabilities [38], while for $\mathrm{Ri}_g < 0$ local overturning can take place.

A relevant timescale for the tracers is the Lagrangian turnover time (or the Lagrangian time)

$$T_L = \int_0^\infty \langle \mathbf{v}_i(t-\tau)\cdot\mathbf{v}_i(t)\rangle d\tau / \langle v_i^2\rangle, \tag{8}$$

where the averages are done over the time t and over all particles (i.e., over the subindex i); T_L quantifies the time over which particles' velocities are autocorrelated. Other relevant parameters for the following sections are the Eulerian turnover time at the Ozmidov scale $\tau_{\mathrm{Oz}} = L_{\mathrm{Oz}}/U_z$ (with U_z the characteristic Eulerian vertical velocity) and the energy-containing (or *integral*) isotropic and parallel length scales

$$L = 2\pi \frac{\int E_V(k) k^{-1} dk}{\int E_V(k) dk}, \tag{9}$$

$$L_\parallel = 2\pi \frac{\int E_V(k_\parallel) k_\parallel^{-1} dk_\parallel}{\int E_V(k) dk}, \tag{10}$$

where $E_V(k)$ and $E_V(k_\parallel)$ are, respectively, the isotropic and parallel kinetic energy spectra. From these lengths we can also define an energy-containing isotropic wave number as $K = 2\pi/L$ and an energy-containing parallel wave number as $K_\parallel = 2\pi/L_\parallel$.

The numerical simulations were performed in three-dimensional periodic domains with different aspect ratios. The first set of runs has a cubic box with domain lengths $L_x = L_y = L_z$ (equal to 2π in dimensionless units) and isotropic linear resolution $n_x = n_y = n_z$ and therefore with an aspect ratio of the vertical to horizontal lengths of 1:1. Another set of simulations was done in elongated boxes of sizes $L_x = L_y = \alpha L_z$ and resolution $n_x = n_y = \alpha n_z$. Thus, the aspect ratio of the domain is $1{:}\alpha$ and we will consider in the following $\alpha = 4$ or 8. Note that in all cases the spatial resolution is isotropic, i.e., the distance between grid points is the same in the three directions $\Delta x = \Delta y = \Delta z$ and thus isotropy can in principle be recovered by the flow at the smallest scales.

In each domain, simulations were done using two different forcing functions. Some simulations were forced with TG forcing (see, e.g., [10,37,39]), which only excites directly the two horizontal components of the velocity field and has vertical shear. The geometry of the large-scale flow generated by this forcing is that of pairs of counterrotating horizontal vortices at large scales and the expression of the forcing is

$$\mathbf{f}_{\rm TG} = f_0(\sin(x)\cos(y)\cos(\alpha z), -\cos(x)\sin(y)\cos(\alpha z), 0). \tag{11}$$

The effectively forced wave number is then $k_f = (2+\alpha^2)^{1/2}$. Note that changing the aspect ratio of the domain modifies the factor $\alpha = L_x/L_z$ and thus the strength of vertical gradients in the flow. For $\alpha = 1$ (cubic domain), $k_f \approx 1.7$, while for $\alpha = 4$ or 8 we obtain, respectively, $k_f \approx 4.2$ or 8.1. The flow generated by these forces (for $\alpha \neq 1$) still has a large-scale circulation at $k_x = k_y = 1$ while developing stronger shear in the vertical direction as α is increased (see [37] for more details).

Other simulations were done using a random isotropic three-dimensional forcing (RND), with a correlation time $\tau_{\rm corr}$ of half an eddy turnover time. A forcing with random phases in the Fourier shell $k_f = \alpha$ is computed at a given time as

$$\mathbf{f}_1 = f_0 \sum_{|\mathbf{k}|\in[k_f,k_f+1)} {\rm Re}(i\mathbf{k}\times\hat{\mathbf{u}}_\mathbf{k} e^{i(\mathbf{k}\cdot\mathbf{r}+\varphi_\mathbf{k})}), \tag{12}$$

where Re stands for the real part, $\hat{\mathbf{u}}_\mathbf{k}$ is a unit vector, and $\varphi_\mathbf{k}$ are uniformly distributed random phases. The actual forcing $\mathbf{f}_{\rm RND}$ is obtained by slowly interpolating the forcing from a previous random state $\mathbf{f}_0$ to the new random state $\mathbf{f}_1$ in such a way that $\mathbf{f}_{\rm RND} = \mathbf{f}_1$ after $\tau_{\rm corr}$. The process is then repeated to obtain a slowly evolving random forcing. As the forcing wave number depends on the aspect ratio, in the cubic box $k_f = 1$, while in the elongated domains $k_f = 4$ or 8, similarly to the Taylor-Green case. However, note that in this case the choice $k_f = \alpha$ to maintain the forcing isotropic for all aspect ratios also implies that, as the aspect ratio $1{:}\alpha$ is decreased and the forcing is applied (isotropically) at smaller scales, the Reynolds number (based on the energy-containing scale) will also decrease.

All flows were evolved from $\mathbf{u} = \theta = 0$, and once they reached the turbulent steady state, Lagrangian particles were injected and integrated in time together with the flow. The list of all runs with their respective relevant parameters is presented in Table I. Runs are labeled using the forcing (TG or RND), a subindex for the inverse aspect ratio ($\alpha = 1$, 4, or 8), and a number indicating the value of the Brunt-Väisälä frequency ($N = 4$, 8, or 12). As mentioned above, note that run $\rm RND_4 8$ has a lower Re than, e.g., run $\rm TG_4 8$ (although it has the same spatial resolution and kinematic viscosity), as the isotropic forcing at $k_f = \alpha = 4$ in the $\rm RND_4 8$ run results in a smaller integral length scale when compared to the $\rm TG_4 8$ run, which has a large-scale flow at horizontal scales (with $k_\perp \approx 1$) with shear at smaller vertical scales (with $k_\parallel = 4$). However, note that run $\rm RND_4 8$ also has a larger Fr, thus resulting in a larger Rb. To explore the effect of varying Re and Rb while keeping the forcing and aspect ratio fixed and Fr approximately the same, runs $\rm RND_4 8$ and $\rm RND_4 8B$ to $\rm RND_4 8D$ were done at decreasing spatial resolution and at increasing values of $\nu = \kappa$.

TABLE I. Relevant parameters of the simulations. The aspect ratio gives the vertical to horizontal aspect ratio of the spatial domain 1:α; n_x, n_y, and n_z are the grid points in each spatial direction; forcing indicates the forcing function; Re is the Reynolds number; Fr is the Froude number; Rb is the buoyancy Reynolds number; R is the fraction of particles with $\mathrm{Ri}_g < 0$; L_{Oz} is the Ozmidov length scale; and $\tau_{\mathrm{Oz}} = L_{\mathrm{Oz}}/U_z$ is the Eulerian turnover time at the Ozmidov scale.

Run	Aspect ratio	$n_x = n_y$	n_z	Forcing	N	Re	Fr	R_b	R	$2\pi/N$	L_{Oz}	τ_{Oz}
$\mathrm{TG}_1 4$	1:1	512	512	TG	4	7000	0.04	11	0.12	1.57	0.28	1.2
$\mathrm{TG}_1 8$	1:1	512	512	TG	8	8000	0.02	3	0.03	0.79	0.1	0.8
$\mathrm{TG}_4 4$	1:4	768	192	TG	4	10000	0.05	25	0.25	1.57	0.36	1.4
$\mathrm{TG}_4 8$	1:4	768	192	TG	8	14000	0.03	13	0.09	0.79	0.14	0.7
$\mathrm{TG}_4 12$	1:4	768	192	TG	12	15000	0.02	4	0.03	0.52	0.07	1.0
$\mathrm{TG}_8 8$	1:8	2048	256	TG	8	35000	0.03	30	0.30	0.79	0.18	0.8
$\mathrm{RND}_1 4$	1:1	512	512	RND	4	6000	0.07	29	0.06	1.57	0.24	0.9
$\mathrm{RND}_1 8$	1:1	512	512	RND	8	8000	0.03	7	0.02	0.79	0.07	0.3
$\mathrm{RND}_4 8$	1:4	768	192	RND	8	3000	0.11	36	0.16	0.79	0.17	0.7
$\mathrm{RND}_4 8\mathrm{B}$	1:4	512	128	RND	8	2000	0.10	20	0.07	0.79	0.14	0.6
$\mathrm{RND}_4 8\mathrm{C}$	1:4	256	64	RND	8	800	0.17	23	0.02	0.79	0.16	0.8
$\mathrm{RND}_4 8\mathrm{D}$	1:4	128	32	RND	8	300	0.20	12	0.25	0.79	0.15	0.2

III. SINGLE-PARTICLE VERTICAL DISPERSION IN STABLY STRATIFIED TURBULENCE

Particle dispersion in SST is inherently different from HIT as stratification suppresses vertical dispersion. As mentioned in the Introduction, linear models of SST predict the saturation of the vertical dispersion for $t \approx 2\pi/N$, as the displacement of particles is in practice vertically bounded by the stratification, resulting in an oscillatory motion of the particles [28]. This is confirmed by numerical simulations at moderate buoyancy Reynolds number [5,12].

We computed the single-particle vertical dispersion as $\delta z^2 = \langle [z_i(t) - z_i(0)]^2 \rangle_i$, where i is the particle label and the average is computed over all particles. Figure 1 shows the resulting mean

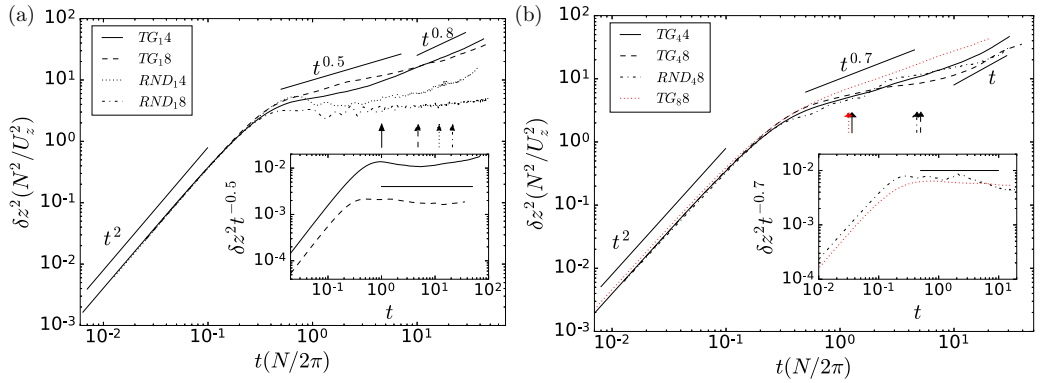

FIG. 1. Mean vertical dispersion δz^2 for (a) runs in cubic domains (boxes with aspect ratio 1:1) and (b) runs in elongated domains with aspect ratio 1:4, in both figures with TG and RND forcing and with different Brunt-Väisälä frequencies. The dispersion is normalized by U_z^2/N^2, the ratio of the squared mean vertical velocity to the Brunt-Väisälä frequency, and time is normalized by the Brunt-Väisälä period. Power laws are indicated as references. In each figure, the Lagrangian time of each run is indicated by a vertical arrow with the same line style as the corresponding run, while the insets show the mean vertical dispersion of some of the simulations, not normalized, and compensated by the power laws indicated in the main panels for intermediate times.

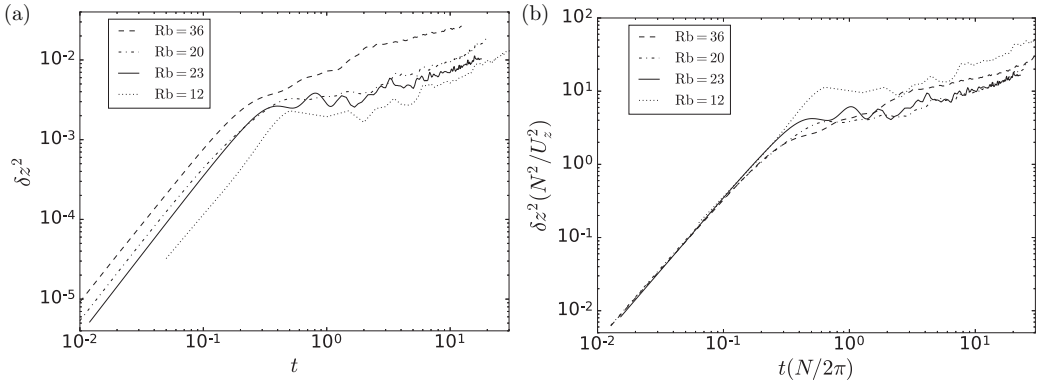

FIG. 2. Mean-square vertical displacement δz^2 for RND runs in domains with aspect ratio 1:4 and with $N = 8$ (run $\mathrm{RND}_4 8$ and runs $\mathrm{RND}_4 8\mathrm{B}$ to $\mathrm{RND}_4 8\mathrm{D}$, from higher to lower Re and Rb): (a) $\delta z^2(t)$ without normalization and (b) same as (a), normalized by the ratio U_z^2/N^2 and with time normalized by the Brunt-Väisälä period.

vertical dispersion in our simulations, for TG and RND forcing, different aspect ratios, and different Brunt-Väisälä frequencies (and thus different Froude numbers). Time is normalized by $2\pi/N$ (the Brunt-Väisälä period), while δz^2 is normalized by $(U_z/N)^2$ (following the normalization used in Ref. [29]), where U_z is, as already mentioned, the (Eulerian) rms vertical velocity in the turbulent steady state when the particles were injected in the flow (note that while U_z does not change significantly in time and has similar values for both forcing functions, the pointwise value of u_z changes significantly in space in the runs with TG forcing, as will be discussed in detail in Sec. IV B). With this normalization all curves collapse from $t = 0$ until $t \approx 2\pi/N$, in a time range when they display ballistic behavior $\delta z^2 \sim t^2$. In Fig. 1 we also indicate with arrows the Lagrangian time T_L of each simulation. These times are very different for each run and are also different from the time at which the ballistic behavior ends. The end of the ballistic regime at the time of the wave period $2\pi/N$, instead of at the Lagrangian time T_L, indicates that the early-time fast vertical dispersion is dominated by the waves, in good agreement with previous studies of SST [11,29]: Particles are first displaced ballistically by the internal gravity waves, which for $\mathrm{Fr} < 1$ are faster than the large-scale turbulent eddies.

The ballistic behavior observed in Fig. 1 finishes after one Brunt-Väisälä period, resulting in a change in the growth of $\delta z^2(t)$. In some cases (see runs $\mathrm{RND}_1 4$ and $\mathrm{RND}_1 8$ in Fig. 1) $\delta z^2(t)$ grows very slowly or even saturates at late times, displaying a plateau. The saturation was reported before in simulations of SST at moderate Re and Rb numbers [11,29], where a very slow growth at late times was attributed to the effect of molecular diffusion. However, some of our runs (all TG runs even at moderate Rb and simulations with RND forcing at higher Rb in elongated domains) display a more efficient transport [i.e., a faster growth of $\delta z^2(t)$ for $t > 2\pi/N$] when compared with the runs that display the plateau. The enhanced dispersion after $t > 2\pi/N$ seems to be controlled, at least for RND forcing, by Rb, suggesting it may be caused by turbulence generated by shear instabilities or by overturning events. As a reference, some power laws are shown in Fig. 1 in this late-time regime and the mean vertical dispersions of some of the simulations, compensated by these power laws, are shown in insets. However, note that, as will be discussed in Sec. V, the enhanced dispersion seen in some of these runs is a combination of the effects of both the waves and the turbulent eddies and as a result it is not captured by a unique power law and tends in some of the runs (at sufficiently high Rb or for sufficiently strong overturning events) to a $\delta z^2 \sim t$ behavior for sufficiently long times.

To further illustrate the effect of varying Rb, Fig. 2 shows the single-particle vertical dispersion for several runs with RND forcing and with the same parameters as $\mathrm{RND}_4 8$ (runs $\mathrm{RND}_4 8\mathrm{B}$ to $\mathrm{RND}_4 8\mathrm{D}$), but with different spatial resolution and values of Rb (by decreasing Re). Run $\mathrm{RND}_4 8\mathrm{D}$,

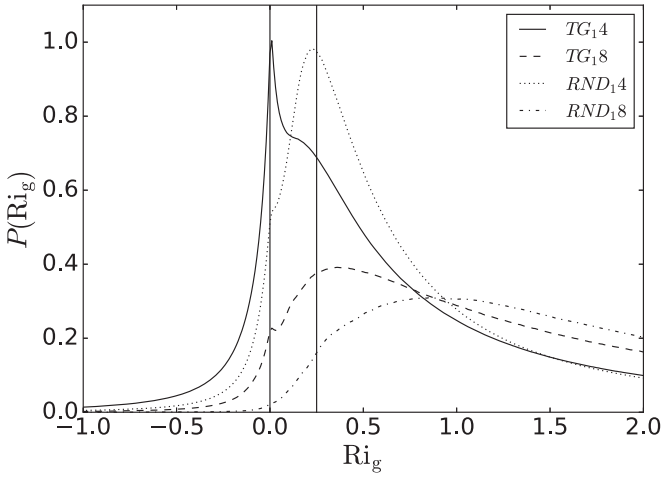

FIG. 3. The PDFs of the Eulerian local gradient Richardson number Ri_g, for all runs in cubic domains (runs $\mathrm{TG}_1 4$ and $\mathrm{TG}_1 8$ with TG forcing and $N = 4$ and 8, respectively, and runs $\mathrm{RND}_1 4$ and $\mathrm{RND}_1 8$ with RND forcing and $N = 4$ and 8, respectively). Vertical solid lines at $\mathrm{Ri}_g = 0$ and $1/4$ are shown as references.

with the lowest values of Re ≈ 300 and of Rb ≈ 12, displays a saturation in $\delta z^2(t)$ at $tN/2\pi \approx 7 \times 10^{-1}$, a plateau until $tN/2\pi \approx 5$, and then a slow growth. As Rb increases the plateau shortens, until it completely disappears for run $\mathrm{RND}_4 8$ (with Re ≈ 3000 and Rb ≈ 36). Note that while Fig. 2(a) shows δz^2 without any normalization (and thus the increase in its amplitude with increasing Rb can be easily appreciated), Fig. 2(b) shows $\delta z^2(N^2/U_z^2)$. In this latter case, the change in the amplitude seen at late times is thus associated with the fact that U_z^2 also increases with increasing Rb, resulting in a net decrease of $\delta z^2(N^2/U_z^2)$ with increasing Rb. However, this normalization (together with the normalization of the time t by the Brunt-Väisälä period) makes all curves collapse again at early times, further showing that the ballistic behavior is independent of Rb and thus of the strength of the small-scale turbulence.

The case of TG forcing is different, as the plateau in $\delta z^2(t)$ at intermediate times is not present even in runs at moderate Rb. Although turbulence plays an important role in the dispersion at high Rb, the TG forcing function generates a coherent large-scale flow which creates strong fronts and helps instabilities to develop [37], enhancing vertical dispersion even at values of Rb which are low when compared to the RND case. In the next section we study the gradient Richardson number Ri_g, with a special focus on the TG simulations, to characterize the features of this flow that result in differences in the vertical dispersion.

IV. LOCAL GRADIENT RICHARDSON NUMBER

A. General properties of the local gradient Richardson number

The local gradient Richardson number provides a measure of the vertical stability of stratified flows. When $\mathrm{Ri}_g(\mathbf{r}) < 1/4$ pointwise, local shear instabilities can take place [40], while if $\mathrm{Ri}_g < 0$, then $\partial_z \theta > N$ and an overturning instability can develop generating convection locally in the flow. Figure 3 shows the probability density functions (PDFs) of the Eulerian Ri_g for all runs in cubic domains. The PDFs of runs with $N = 4$ ($\mathrm{TG}_1 4$ and $\mathrm{RND}_1 4$) display larger probabilities of low values of Ri_g (less than $1/4$ and less than 0) than the runs with the same forcing but with $N = 8$ ($\mathrm{TG}_1 8$ and $\mathrm{RND}_1 8$). As N is increased (for a given forcing), the peak of the PDF moves to larger values of Ri_g. This indicates, as expected, that as stratification increases vertical instabilities are inhibited and as a result we can also expect a less efficient vertical transport (in agreement with the

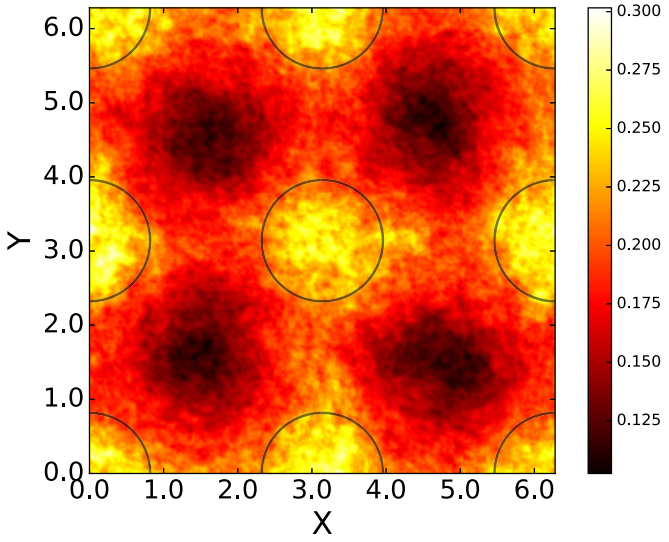

FIG. 4. Vertically averaged absolute value of the Eulerian vertical velocity $\langle|u_z|\rangle_z$ for run $TG_4 4$ (TG forcing, $N = 4$, and aspect ratio 1:4). Bright regions correspond to large vertical velocities in absolute value. As the domain is periodic in both the x and y directions, the regions with large $\langle|u_z|\rangle_z$ can be enclosed by four circles (cylinders when extended in the z direction), indicated as a reference by the black solid lines.

single-particle vertical dispersion observed in the preceding section). However, when we compare TG and RND runs with the same value of N, we see that TG runs still show larger probabilities of $\mathrm{Ri}_g < 1/4$ and of $\mathrm{Ri}_g < 0$. Indeed, the PDFs of the TG runs are shifted towards the left relative to the RND set, indicating that this flow is more vertically unstable and consequently can be more efficient at vertically displacing particles.

B. Spatial structure of the local gradient Richardson number in the TG flow

We are interested in how the TG forcing affects the structure of the local gradient Richardson number. As the forcing generates a coherent large-scale flow, which in principle can affect vertical transport, we show first in Fig. 4 the mean vertical value of the absolute Eulerian vertical velocity $\langle|u_z|\rangle_z$ computed for run $TG_4 4$ (where the subscript z in the brackets indicates the average was computed along the z coordinate). As explained in Sec. II, the TG flow consists of pairs of counterrotating horizontal vortices, separated vertically by shear layers. Pressure gradients create a vertical circulation [37] and as a result the forcing generates a coherent structure at the largest scales that organize the flow into regions of high and low $\langle|u_z|\rangle$. As a result, some well-defined spatial regions in the flow display a bias towards larger values of $|u_z|$ (also associated with the generation of frontlike and filamentlike structures in the flow, as discussed in Ref. [37]). As a comparison, the runs with RND forcing do not display such a large-scale structure (not shown). It can thus be expected that Lagrangian particles approaching these regions in the TG flow will have a tendency to suffer larger displacements in the vertical direction, thus increasing δz^2 even at moderate Rb.

To confirm this effect, Fig. 5 shows the PDFs of the Lagrangian Ri_g (i.e., now computed using the gradients as seen by the Lagrangian particles) for runs with TG forcing in the box with 1:4 aspect ratio. Gradients (as well as velocity and density fluctuations) seen by the Lagrangian tracers are computed for each time and at each particle position using the same three-dimensional cubic spline interpolation used to integrate the particles discussed in Sec. II. From these quantities, the PDFs of Ri_g are computed. As expected, the Lagrangian PDFs coincide with the Eulerian PDFs, which are computed at a fixed time and for all points in the Eulerian spatial grid; however, the PDFs

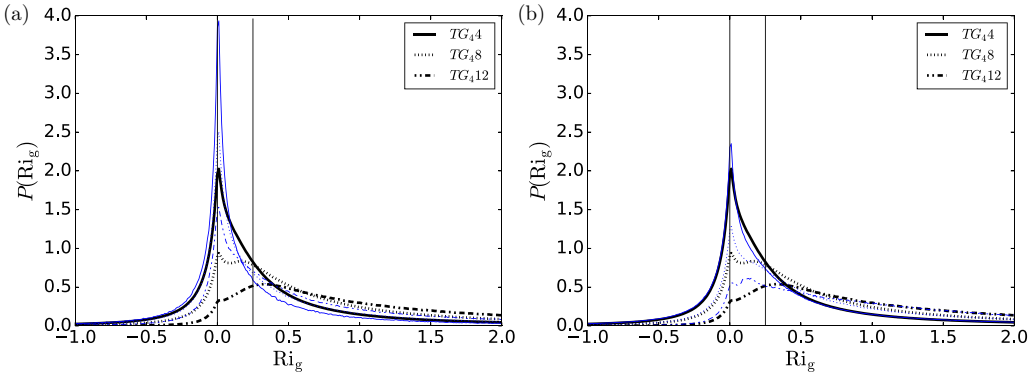

FIG. 5. Thick black lines show the Lagrangian PDFs of the gradient Richardson number Ri_g for TG runs in boxes with 1:4 aspect ratio. This PDF is compared with (a) the PDFs of Ri_g restricted to Lagrangian velocities $|v_z| > \langle |v_z| \rangle + 2\sigma_{v_z}$ (where σ_{v_z} is the dispersion in v_z), shown as thin blue lines, and (b) the PDFs of Ri_g restricted to particles in the circular regions indicated in Fig. 4. Vertical lines at $\mathrm{Ri}_g = 0$ and $\mathrm{Ri}_g = 1/4$ are shown as references.

from Lagrangian data will allow us next to more easily compute statistics restricted to specific conditions over the fluid elements. As a result, as observed before for the Eulerian statistics, for the complete data set, as the stratification increases (i.e., for higher N) the mean gradient Richardson number also increases and the fraction of fluid elements with $\mathrm{Ri}_g < 1/4$ or $\mathrm{Ri}_g < 0$ (i.e., prone to overturning) decreases. However, as we just mentioned, the computation of Ri_g using the gradients as seen by the Lagrangian particles also allows us to compute conditional statistics, e.g., only for instants when the particles suffer large vertical velocities or when the particles are in a specific region in space. Using the mean of the absolute Lagrangian vertical velocity $\langle |v_z| \rangle$ (averaged over all particles and over time) and the standard deviation of v_z (σ_{v_z}), we computed the PDF of Ri_g restricted to particles with absolute vertical velocity $2\sigma_{v_z}$ larger than $\langle |v_z| \rangle$ (see Fig. 5). With this restriction, the fraction of fluid elements that can suffer overturning instabilities increases (note the PDFs have a larger peak at $\mathrm{Ri}_g = 0$ and display larger values for $\mathrm{Ri}_g < 0$ and smaller values for $\mathrm{Ri}_g > 0$ when compared with the PDFs at the same N without any restriction). This indicates that there is a correlation between fluid elements with $\mathrm{Ri}_g \leqslant 0$ and large values of $|v_z|$ (and thus of particles displacing larger distances in the vertical direction and contributing to δz^2). We also see that as N is increased, the probability of finding fluid elements with $\mathrm{Ri}_g \leqslant 0$ decreases even when restricted to parcels with large $|v_z|$. Finally, Fig. 5 also shows the PDF of Ri_g restricted to the instants the particles are in the spatial regions of the large-scale circulation for which the largest absolute values of u_z were observed in Fig. 4. A similar (albeit weaker) behavior as for the restriction in v_z is found, with the shift in the peak of the PDFs towards smaller values of Ri_g, confirming the relevance of the geometry of the large-scale flow in the TG runs for the vertical transport of Lagrangian particles.

To further study the effect of Ri_g on the vertical velocity of the particles, Fig. 6 shows the PDFs of the Lagrangian vertical velocity for all particles in TG runs with aspect ratio 1:4 and with varying N. As previously reported in Refs. [15,16], the vertical velocity does not follow Gaussian statistics and displays strong tails (this feature is not exclusively associated with the TG forcing, as the same behavior was found in simulations with random forcing, see [15]). In Ref. [16] the extreme values were shown to be associated with intermittent overturning instabilities in the flow. Note that the behavior reported in Ref. [16] is nonmonotonic in Fr, although for sufficiently small Fr (or sufficiently large values of N) the maximum values of v_z decrease with increasing stratification (see Fig. 6). When we compute the PDFs restricted to particles in instants for which $\mathrm{Ri}_g < 1/4$ or $\mathrm{Ri}_g < 0$, while for the runs with moderate stratification ($N = 4$ and 8) there are only small changes in the tails of the PDFs (albeit extreme values of v_z become more probable), for

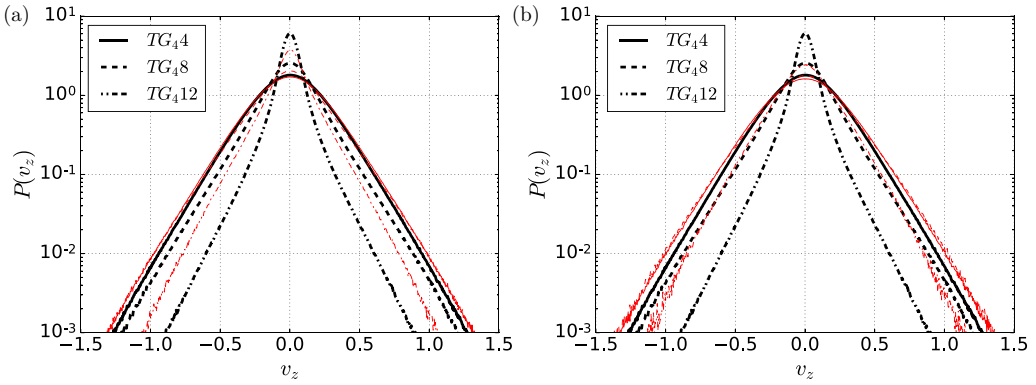

FIG. 6. Thick black lines show the PDFs of the Lagrangian vertical velocity v_z for TG runs in domains with 1:4 aspect ratio and varying N. The PDFs restricted to particles in instants with (a) $\mathrm{Ri}_g < 1/4$ or (b) $\mathrm{Ri}_g < 0$, for the same runs, are shown as thin red lines.

stronger stratification ($N = 12$) the changes are significantly larger, with stronger tails. This further confirms that points with $\mathrm{Ri}_g < 1/4$ or $\mathrm{Ri}_g < 0$ are associated with larger values of v_z and can thus be expected to be associated with the enhanced dispersion after $t > 2\pi/N$ at least in the TG runs.

This can also be confirmed in Fig. 7, which shows the joint probability density function as a function of Ri_g and $|v_z|$, $P(\mathrm{Ri}_g, |v_z|)$, for the TG runs with aspect ratio 1:4 and with varying N. As the stratification increases, the probability of finding particles with large values of $|v_z|$ decreases, while that of finding larger values of Ri_g increases. For $N = 4$ and $N = 8$ note the correlation between larger absolute values of the vertical velocity with $\mathrm{Ri}_g \approx 0$ values, which is significantly weaker in the run with $N = 12$.

Finally, we also studied how the value of Ri_g affects θ and $\partial_z\theta$ with increasing stratification (note that the local value of $\partial_z\theta$ is important for overturning instabilities, as the gradient of the buoyancy fluctuations can compete with the background gradient, resulting in local inversion of the stratification). Figure 8 shows the PDFs of θ as seen by the Lagrangian particles and the same PDFs restricted to instants when $\mathrm{Ri}_g < 1/4$ or $\mathrm{Ri}_g < 0$, in all cases for the TG_4 runs. For $N = 4$ the PDFs of θ are close to Gaussian and the restriction in the values of Ri_g has a negligible effect in the statistics. However, for $N = 8$, while the PDFs are still close to Gaussian, the restricted PDFs show a lower probability for $|\theta| < 0.5$ and higher probability for $|\theta| > 0.5$, indicating that particles with $\mathrm{Ri}_g < 1/4$ or $\mathrm{Ri}_g < 0$ are more likely to be found at points with higher potential energy density $\sim\theta^2$. This behavior is enhanced for $N = 12$, for which the PDFs also display non-Gaussian tails. Finally, Fig. 9 shows the PDFs of the Lagrangian vertical gradients of θ, $\partial_z\theta$, which are non-Gaussian and

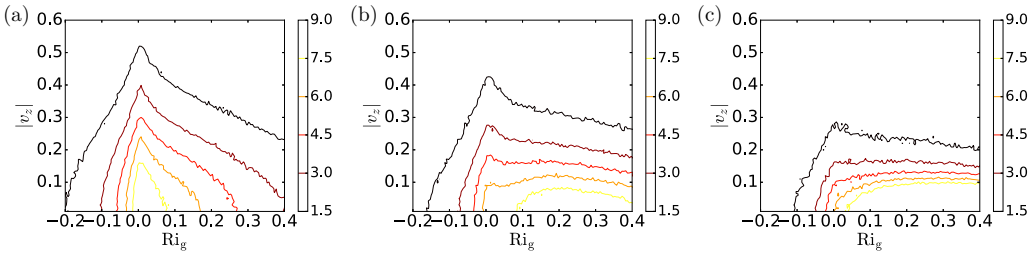

FIG. 7. Isocontours of the joint probability distribution function of Ri_g and $|v_z|$, $P(\mathrm{Ri}_g, |v_z|)$, for runs (a) $\mathrm{TG}_4 4$, (b) $\mathrm{TG}_4 8$, and (c) $\mathrm{TG}_4 12$.

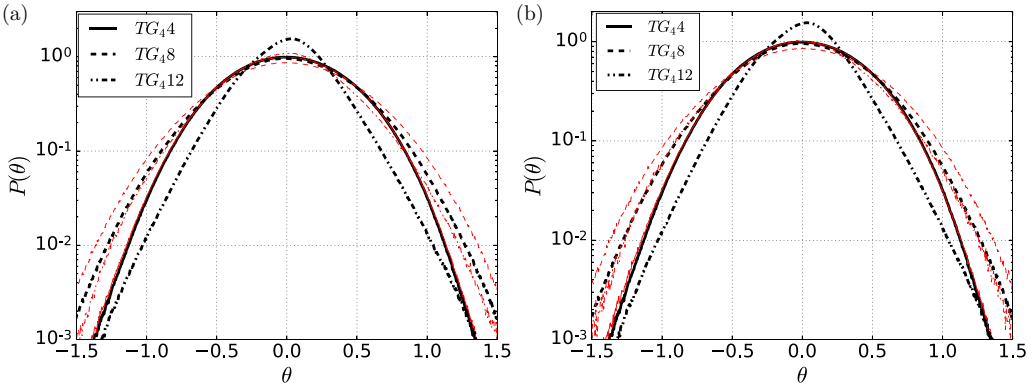

FIG. 8. The PDFs of θ as seen by the Lagrangian particles (thick black curves) and the same PDFs restricted (thin red curves) to (a) particles at times with $\mathrm{Ri}_g < 1/4$ and (b) particles at times with $\mathrm{Ri}_g < 0$. Except for the run $\mathrm{TG}_4 12$, all PDFs are compatible with Gaussian statistics for θ.

asymmetric. The asymmetry is enhanced when the PDFs are restricted to instants when $\mathrm{Ri}_g < 1/4$ or $\mathrm{Ri}_g < 0$. While the nonrestricted PDFs have their maximum at $\partial_z\theta \gtrsim 0$, for the restricted PDFs the maximum is at $\partial_z\theta \approx N$. From the ideal Boussinesq equation for θ [Eq. (2), with $\kappa = 0$], it can be seen that $\nabla\theta = (0, 0, N)$ is a fixed point of the equations for both θ and the Lagrangian evolution of $\partial_z\theta$, which could explain the accumulation of (restricted) particles with $\partial_z\theta \approx N$. Also, at points where $\mathrm{Ri}_g < 0$, then $\partial_z\theta > N$ (for which overturning events can occur). This is the reason why the PDFs of particles restricted to $\mathrm{Ri}_g < 0$ in Fig. 9 only take values of $\partial_z\theta$ greater than N. Finally, note that since Ri_g depends explicitly on $\partial_z\theta$ and not on the pointwise value of θ, a restriction on the values of Ri_g can be expected to affect the PDFs in Fig. 9 more strongly than those in Fig. 8, as is indeed observed in the figures.

C. Overturning probability and the buoyancy Reynolds number

As already mentioned, the extreme vertical velocities reported in the preceding section are not exclusive to the TG flow. In Refs. [15,16], non-Gaussian PDFs of u_z, v_z, and θ were reported for RND forcing depending on the values of Fr and Rb. However, it is clear from the results shown so

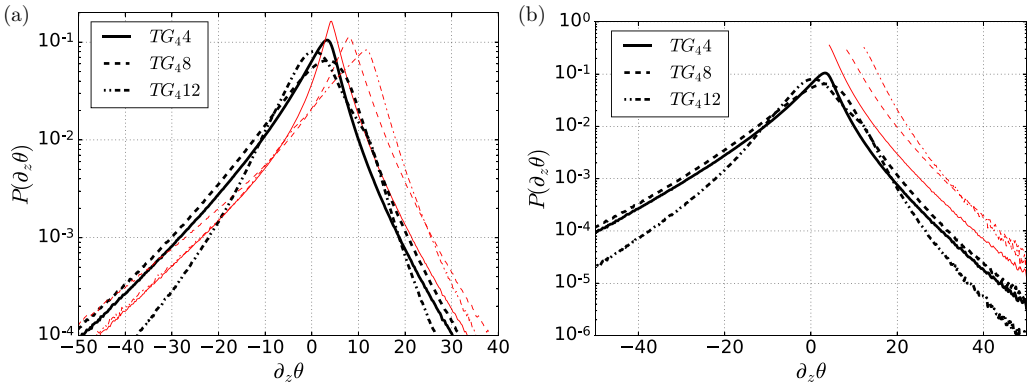

FIG. 9. The PDFs of the Lagrangian vertical temperature gradients $\partial_z\theta$ (thick black curves) and the same PDFs restricted (thin red curves) to (a) $\mathrm{Ri}_g < 1/4$ and (b) $\mathrm{Ri}_g < 0$.

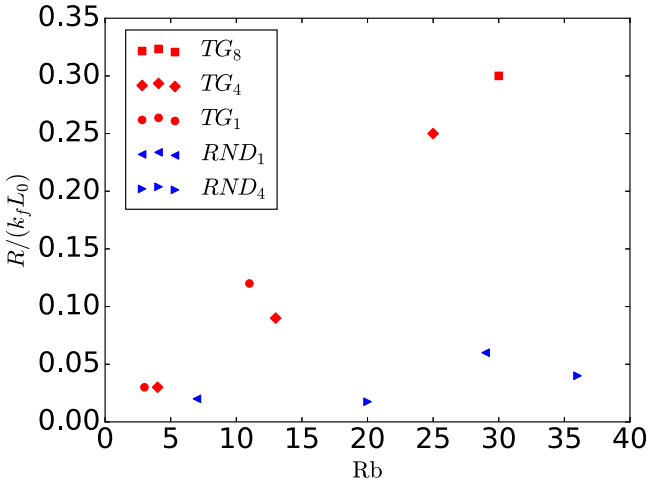

FIG. 10. Overturning probability normalized by the forcing wave number and unit length, $R/k_f L_0$, as a function of the Reynolds buoyancy number Rb for all simulations in Table I.

far that the geometry of the TG flow facilitates the development of overturning instabilities and the occurrence of extreme values of the vertical velocity even at moderate Rb.

In the next section we will use these results to build a simple model for single-particle vertical dispersion, for all cases considered and independently of the two specific forcing function used. The results in Sec. III suggest that while the ballistic behavior of δz^2 for $t < 2\pi/N$ is dominated by the waves, the differences in δz^2 for $t > 2\pi/N$ depend on the strength of the vertical velocity and of the turbulence. For moderate turbulence (i.e., moderate values of Rb) and without a large-scale vertical circulation, δz^2 is dominated by the waves even at late times, resulting in the observed saturation of the single-particle vertical dispersion. However, for larger values of Rb (as in some of the RND runs) or in the presence of a large-scale flow (as in all TG runs), strong vertical updrafts or downdrafts can enhance vertical transport resulting in the growth of δz^2 at late times. We will measure the probability of this happening by introducing an overturning probability R, defined as the fraction of particles (in the Lagrangian frame) or the fraction of space volume (in the Eulerian frame) with $\mathrm{Ri}_g < 0$. Figure 10 (see also Table I) gives $R/k_f L_0$ as a function of Rb for all runs, where R is measured as the integral of the PDF of Ri_g for $\mathrm{Ri}_g < 0$. The normalization of R by the product $k_f L_0$ (where k_f is the forcing wave number and L_0 the unit length) makes all simulations with a given forcing (either RND or TG) collapse in the vicinity of approximate linear relations independently of the forcing wave number used. Indeed, the data follow (for the range of Rb considered) a linear relation with Rb, with two different slopes for the TG and RND runs (even when the runs in each set also have different aspect ratios, forcing wave numbers, Reynolds, and Froude numbers). As expected, for fixed Rb, the TG runs display larger values of R than the RND runs.

V. SINGLE-PARTICLE VERTICAL DISPERSION MODEL

To study the vertical dispersion of single-particles observed in the DNSs of SST in Sec. III, we now present a stochastic model that combines a random wave model (to consider the effect of internal gravity waves) with a CTRW [41] (to capture the effect of overturning by turbulent or large-scale eddies). Based on the results presented so far (and in particular on the observation that at early times the behavior is dominated by waves), the wave model we present consists of a sum of linear waves with random phases. The presence of internal gravity waves in these flows and their dispersion relation have been studied before in spatiotemporal studies (see, e.g., [10]), further indicating their relevance in the dynamics of SST. We can thus approximate the trajectory of a

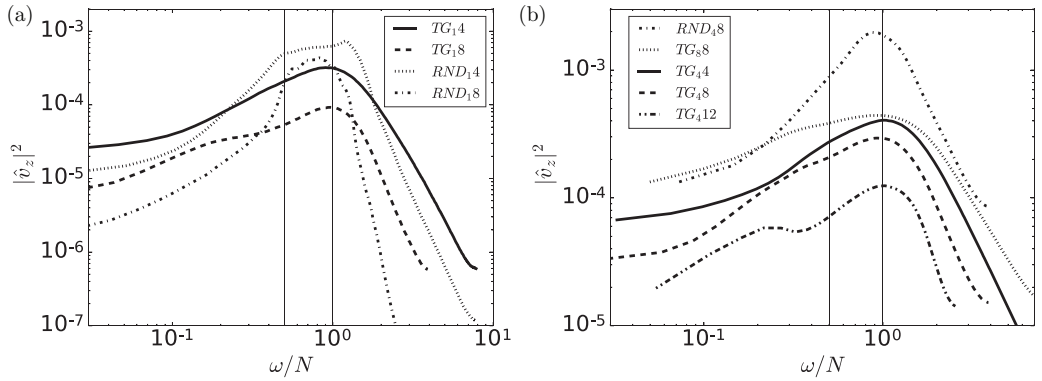

FIG. 11. Power spectrum of the Lagrangian vertical velocity for (a) runs in cubic domains and (b) runs in elongated domains. Frequencies have been normalized by the Brunt-Väisälä frequency. The solid vertical lines indicate (from left to right) $\omega = N/2$ and $\omega = N$.

Lagrangian particle moving vertically following these waves as

$$z_{\rm wav}(t) = {\rm Re}\left(\sum_{\omega} A_\omega e^{i(\omega t+\phi_\omega)}\right), \tag{13}$$

where ϕ_ω is a random phase (note that, as we are interested only in the vertical motion of the particles, the possible dependence of traveling waves on x and y can be ignored or absorbed into the random phase) and the sum is performed over N_ω uniformly distributed frequencies in the range of frequencies $\omega \in [\omega_{\rm min}, \omega_{\rm max}]$. The amplitude of the waves satisfies the spectral relation

$$A_\omega = A_0 \omega^{-1} \tag{14}$$

for the same range of frequencies and where A_0 is a normalization factor. The dependence of $A_\omega \sim \omega^{-1}$ follows from observations that the power spectrum of the actual Lagrangian vertical velocity has a broad maximum with approximately constant amplitude near the Brunt-Väisälä frequency. Note that associating v_z with $\dot{z}_{\rm wav} = {\rm Re}(\sum A_\omega \omega e^{i(\omega t+\phi_\omega)})$, a flat power spectrum for v_z implies Eq. (14) for the amplitude of the waves. Once N_ω is chosen, the normalization factor A_0 can then be fixed as $A_0 = (2U_z^2/N_\omega)^{1/2}$ by imposing that for each particle $\langle \dot{z}^2_{\rm wav}\rangle_t$ (averaged over time) must be equal to the mean-square Eulerian vertical velocity U_z^2 (also equal to the mean-square Lagrangian vertical velocity) using Parseval's theorem.

Note also that a flat Lagrangian spectrum for a range of frequencies is compatible with oceanic observations of the so-called Garrett-Munk spectrum and also with numerical simulations of SST [11]. As an example, Fig. 11 shows the power spectrum of the Lagrangian vertical velocity for all runs in Table I. There is a broad peak near $\omega = N$, and in several of the runs an approximately flat spectrum can be observed in its vicinity (as a reference, the figure indicates a range of frequencies $[N/2, N]$), with a decay compatible with a power law for $\omega > N$ and a slowly decaying, or almost flat, spectrum for $\omega \ll N$. Also, for the runs with the smallest values of Rb considered in this study (run TG_18 with Rb = 3.2 and run TG_412 with Rb = 4.3), a secondary peak at smaller frequencies can be observed. In these runs turbulence is moderate and the waves dominate the dispersion at intermediate times.

As the dispersion relation of internal gravity waves is $\omega = Nk_\perp/k \leqslant N$, we set $\omega_{\rm max} = N$ and for simplicity, from the results in Fig. 11, we set $\omega_{\rm min} = N/2$ in all cases. It then follows from Eq. (13) that the vertical displacement of any particle following the waves is given by

$$\delta z_{\rm wav}(t) = z_{\rm wav}(t) - z_{\rm wav}(0) = \sum_{\omega} A_w[\cos(\omega t + \phi_\omega) - \cos(\phi_\omega)]. \tag{15}$$

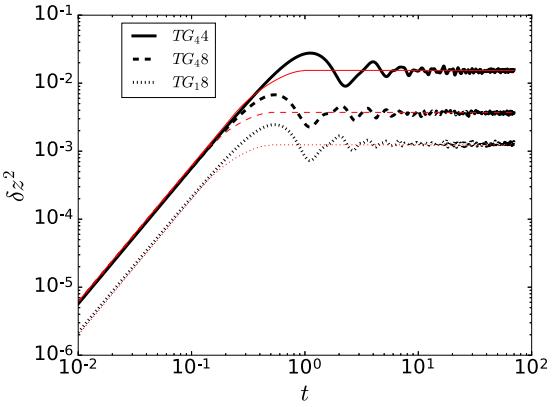

FIG. 12. Mean dispersion obtained from a random superposition of waves as in Eq. (15) (thick black lines) and from Eq. (16) (thin red lines), with the parameter A_0 to match the Eulerian vertical rms velocity and N the Brunt-Väisälä frequency for some of the TG runs (see the labels in the legend).

The square of this expression, when averaged over an ensemble of particles and waves, can be approximated by (see Appendix A)

$$\left\langle \delta z^2_{\rm wav} \right\rangle (t) = \begin{cases} U_z^2 t^2 & \text{if } t \leqslant N^{-1} \\ Q(t) & \text{if } N^{-1} < t < 4N^{-1} \\ \frac{4U_z^2}{N^2} & \text{if } t \geqslant 4N^{-1}, \end{cases} \tag{16}$$

where $Q(t)$ is a third-order polynomial function obtained by imposing $\langle \delta z^2_{\rm wav} \rangle$ and its time derivative to be continuous in time (see Appendix A). Figure 12 shows the mean dispersion for many particles calculated from a stochastic superposition of waves as in Eq. (15) and from the function in Eq. (16), in both cases using values of A_0 and N that adjust the vertical rms velocity and the Brunt-Väisälä frequency of several TG runs. The function in Eq. (16) is in good agreement with the sum of random waves, especially for short and long times. Note also that this simple model, based on a superposition of waves, captures the early-time ballistic behavior of $\delta z^2 \sim t^2$ seen for all DNSs in Fig. 1 as well as the saturation at late times seen in Fig. 1 for some of the simulations.

The behavior shown in Fig. 12 is similar to the vertical dispersion predicted for SST by other models based on a linear superposition of waves [28] and is reminiscent of the vertical dispersion observed in previous DNSs of SST at moderate values of Rb [11,29]. However, this wave model fails to reproduce the dispersion observed at long times in some of our runs. To introduce an enhanced vertical dispersion by turbulent overturning, we add a CTRW model that mimics the trapping of particles by eddies, resulting in vertical displacements when the flow becomes unstable such that the total vertical dispersion will be $\delta z(t) = \delta z_{\rm wav}(t) + \delta z_{\rm CTRW}(t)$.

To compute $\delta z_{\rm CTRW}(t)$, in each step t of the random-walk process we assume that a particle has a probability R of being trapped for a time t_t inside an eddy of radius r_t with velocity U_t. As in the preceding section, R is the probability of finding particles with $\mathrm{Ri}_g < 0$. Whether at a given step t the particle is trapped or not is a binary decision and thus the probability of the particle not being trapped is $1 - R$ (in which case the particle does not move following eddies). When trapped, the probability of being advected by an eddy of radius r_t is given by a Kolmogorov distribution $P(r_t) \sim r_t^{4/3}$ for $r < L_{\rm Oz}$, compatible with an isotropic energy spectrum $\sim k^{-5/3}$ for wave numbers $k > k_{\rm Oz}$; in other words, we assume that the eddies responsible for the vertical dispersion at late times are associated with overturning instabilities in the turbulent inertial range for scales equal to or smaller than the Ozmidov scale. The distribution of trapping times $P(t_t)$ is continuous and uniform between $t_t = 0$ and the Eulerian turnover time at the Ozmidov scale $\tau_{\rm Oz}$. Finally, at each step t and if the particle is trapped, the particle velocity (or, equivalently, the characteristic velocity

of the eddy trapping the particle) is U_t, given by a probability distribution $P(U_t)$ that is obtained from the observed PDF of the absolute value of the Eulerian vertical velocity [which, in practice, can be very well approximated by assuming that it follows a Rayleigh distribution, so knowledge of the rms value of u_z, U_z, is sufficient to estimate $P(U_t)$].

As mentioned above, in each step of the CTRW, if a particle is not trapped by an eddy, $\delta z_{\mathrm{CTRW}}(t)$ will remain constant (i.e., the particle will not move as a result of eddy trapping). If it gets trapped, it will be displaced along a circle as the result of the trapping, with a vertical displacement of $r_t \sin(\theta_t)$ which is just the projection of the circular trajectory of radius r_t in the z direction and where $\theta_t = U_t t_r / r_t$ is the angle of the arc traveled during the time t_r. Thus, the random-walk process just mimics in a simplified way the eventual presence of vertical eddies that can result in upward or downward transport of the Lagrangian particles. As described above, the model has no free parameters; all parameters are obtained from Eulerian characteristic lengths and timescales of the flow.

We can summarize the computation of the entire model as follows.

(1) Wave model. At any time, each particle vertical trajectory is computed as the sum of N_ω harmonic motions, each with amplitude $2U_z^2/N_w\omega$ and with uniformly distributed random frequencies ω between $N/2$ and N.

(2) CTRW model.

(a) At each step t, a particle is trapped by an eddy with probability R (or not trapped, with probability $1 - R$).

(b) If the particle is trapped, (i) the characteristic velocity of the eddy U_t is given by $P(U_t)$, a Rayleigh probability distribution with its mean given by the mean Eulerian vertical velocity of the flow; (ii) the eddy radius r_t is chosen with a probability distribution $P(r_t) \sim r^{4/3}$ for $r_t \leqslant L_{\mathrm{Oz}}$, and $P(r_t) = 0$ in other cases; (iii) the trapping time t_t is chosen from a uniform probability distribution $P(t_t)$ between 0 and τ_{Oz}; (iv) the central angle subtended by the arc traveled by the particle during the trapping time is computed as $\theta_t = U_t t_t / r_t$; and (v) the vertical displacement after the time t_t is finally computed as $r_t \sin(\theta_t)$.

(c) If the particle is not trapped, the particle is not displaced.

(d) The final vertical displacement resulting from the CTRW for any given particle and at a given time $t = \sum_{t=1}^{n} t_t$ is the sum over the n vertical displacements.

(3) Full model. At any given time, the total vertical displacement is obtained as the sum of the displacements generated by the waves and by the CTRW process.

The key parameters of the full model then are N, U_z, L_{Oz}, and R, from which all other variables and probability distributions (as well as the total displacements) can be computed.

Figure 13 shows the mean vertical dispersion obtained from several DNSs and $\delta z^2(t) = [\delta z_{\mathrm{wav}}(t) + \delta z_{\mathrm{CTRW}}(t)]^2$ as obtained from the wave and CTRW model (i.e., the full model). For the runs in elongated domains (with TG forcing or larger values of Rb), as the dispersion is very similar for all runs, we rescaled δz^2 using an arbitrary value [indicated in the legend in Fig. 13(a)], so the curves can be distinguished more easily. In the other cases, the same normalization as in Fig. 1 was used for δz^2 and time. The model is in good agreement with the DNS data in all cases and captures early- and late-time behavior independently of the forcing function (TG or RND), as well as cases with saturation of $\delta z^2(t)$ for $t > 2\pi/N$ as cases in which $\delta z^2(t)$ keeps growing at late times. The inset in Fig. 13(b) shows a detail of the mean vertical dispersion for run $\mathrm{RND}_1 8$ (RND forcing with $N = 8$), for which δz^2 almost completely saturates after $t(N/2\pi) \approx 1$ and grows only very slowly at late times. For this case, the inset also shows δz^2 obtained from the wave model alone (i.e., $\delta z^2_{\mathrm{wav}}$), as well as δz^2 obtained from the full model. This case confirms that while the wave model can capture the saturation, the departure from this saturation and the growth observed at late times can only be captured if trapping by eddies is taken into account.

As mentioned in Sec. III, the apparent power laws observed at intermediate times in Fig. 1 are the result of this competition between dispersion by waves and eddies, and for sufficiently long times δz^2 approaches a linear $\sim t$ behavior if overturning is strong enough. To illustrate this and to show the agreement between the model and the DNSs in more detail, Fig. 14 shows $\delta z^2(t)$ in linear scale for four selected runs (corresponding to cases with TG or RND forcing, with different Brunt-Väisälä

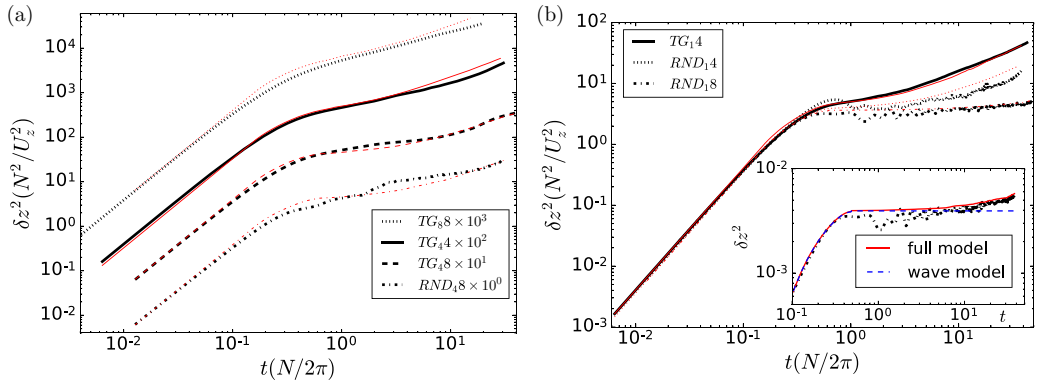

FIG. 13. Mean vertical dispersion δz^2 for (a) runs in elongated domains with amplitudes rescaled for better visualization (see the legend) and (b) runs in cubic domains, for RND and TG forcing and with different values of N. Normalizations of δz^2 and of time are the same as in Fig. 1. In both (a) and (b) the thick black lines show the results from the DNSs and the thin red lines show the results obtained from the single-particle dispersion model. The inset in (b) shows a close-up of δz^2 for run $\mathrm{RND}_1 8$ (thick dash-dotted curve) together with the mean-square vertical displacement predicted by the full model and by the superposition of random waves alone.

frequencies, and with different domain aspect ratios). Considering the inherent randomness of the DNSs results and of the CTRW process, reasonable agreement is seen in all cases.

The differences between the early- and late-time behavior can now be further clarified using the model (see Fig. 15). At early times, the waves dominate the dispersion resulting in the observed ballistic regime up to the period of the slowest waves, $t \lesssim 2\pi/N$, for which the largest "fast" displacements (on the timescale of the waves) can take place. If considered alone, trapping by turbulent eddies in the CTRW model would also result in ballistic growth of δz^2, but it has an initial value significantly smaller and as a result this process is subdominant to the dispersion by the waves. At intermediate times ($t \approx 2\pi/N$) dispersion by the waves saturates generating the plateau. If turbulence is moderate (and thus R is also moderate), trapping by eddies is inefficient, resulting in a temporary saturation of the dispersion, or, in the most extreme cases, in a complete saturation of δz^2. Depending on how strong the turbulence is, at a certain time overturning events can start enhancing the dispersion and for longer times the turbulence dominates the dynamics surpassing the effect of the waves. Remarkably, this simple picture is also compatible with the trajectories of individual Lagrangian particles. Figure 15 also shows as an example four trajectories projected into the x-z plane, for four Eulerian eddy turnovers and for run $\mathrm{TG}_4 4$. Small and wavy displacements can be seen in the vertical direction, interrupted by sudden and close to circular trajectories associated with trapping by overturning eddies and which result in larger vertical displacements.

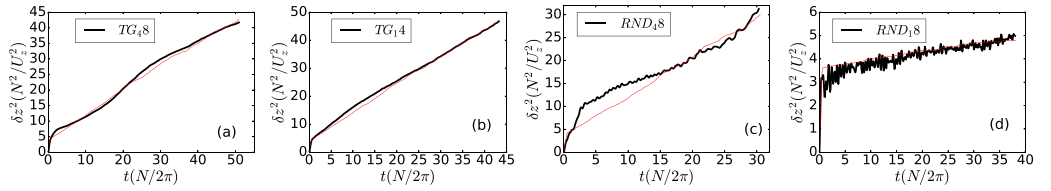

FIG. 14. Mean-square vertical displacement δz^2 in linear scale for four cases: (a) $\mathrm{TG}_4 8$, (b) $\mathrm{TG}_1 4$, (c) $\mathrm{RND}_4 8$, and (d) $\mathrm{RND}_1 8$. The four cases are illustrative of runs with TG or RND forcing, with different levels of stratification and with different domain aspect ratios. The thick black curves show the results from the DNSs, while the thin red lines show the results obtained from the model. In spite of the randomness in the DNSs and in the CTRW model, all cases display reasonable agreement.

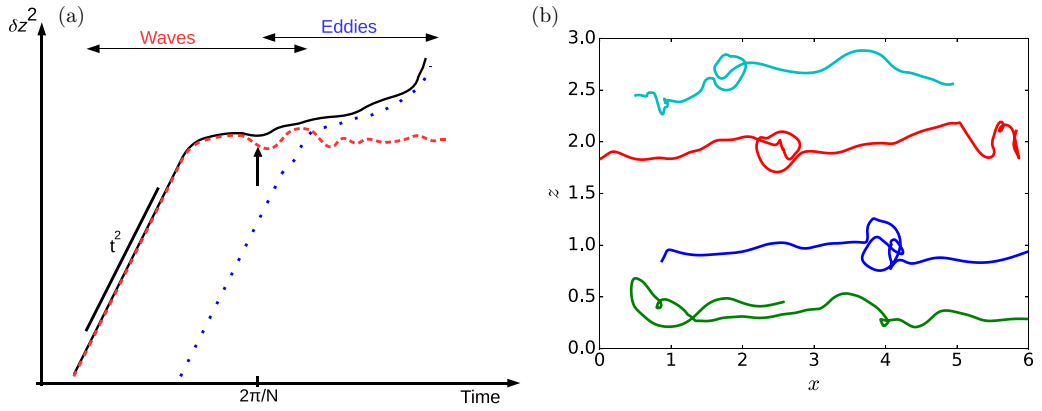

FIG. 15. (a) Sketch of the two contributions to vertical dispersion in the model. The random superposition of waves dominates at early times (red dashed curve), while the effect of turbulent eddies and overturning events become relevant at late times (blue dotted curve). The total vertical dispersion (black solid curve) results from the superposition of both effects. (b) A few particle trajectories from the $TG_4$4 run projected on the x-z plane. Note the small and wavy particles' displacements in the vertical directions, interrupted by sudden and close to circular trajectories that result in a larger vertical displacement, which we associate by trapping by overturning eddies (see Sec. V for details).

VI. TWO-PARTICLE VERTICAL DISPERSION

We can also study the two-particle vertical dispersion ζ_z^2, which the two simple processes presented above (dispersion by a random superposition of waves and a CTRW process to capture the effect of turbulent overturning events) can also model. The two-particle vertical dispersion is defined as $\zeta_z^2 = \langle [z_i(t) - z_j(t)]^2 \rangle_{(i,j)}$, where $i \neq j$ are the labels of two particles that at the initial time have a vertical separation δz_0 and a horizontal separation δr_0 and where the subindex (i, j) denotes that the average is computed over pairs of particles. Figure 16 shows the resulting two-particle

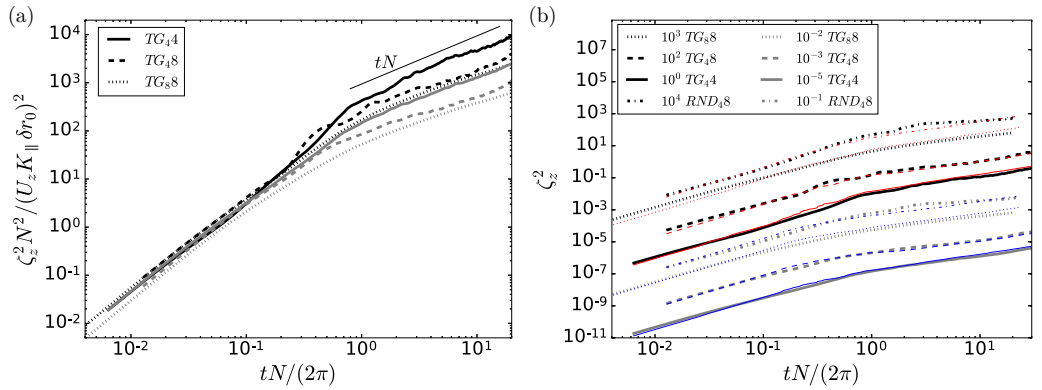

FIG. 16. (a) Two-particle vertical dispersion for particles with initial vertical separation $\delta z_0 \ll \eta$ and two initial horizontal separations $\delta r_0 = \eta$ (black lines) $\delta r_0 = 2\eta$ (gray lines). Results from three simulations with TG forcing are shown. The vertical dispersion was normalized by $(wK_\parallel \delta r_0)^2/N^2$ and time by $1/N$. With this normalization all curves collapse during the ballistic regime. A power law at later times is indicated as a reference. (b) Two-particle vertical dispersion from DNSs with RND or TG forcing (thick lines) and from the model (thin lines). The amplitudes of the curves have been rescaled for better visualization (see the rescaling factor in the legend).

vertical dispersion for runs $TG_4 4$, $TG_4 8$, and $TG_8 8$. We consider pairs of particles which at time $t = 0$ have a vertical separation $\delta z_0 \ll \eta$ (where η is the Kolmogorov dissipation scale) and horizontal separations $\delta r_0 \approx \eta$ or $\delta r_0 \approx 2\eta$ (see [29] for a detailed study of different choices of the initial separation in two-particle dispersion in SST). Normalizing the vertical dispersion ζ_z^2 by $(U_z K_\parallel \delta r_0)^2/N^2$, all curves approximately collapse during the ballistic regime. As for the case of single-particle dispersion, we see again a growth of the two-particle dispersion at late times, which is linear or almost linear with t in all runs. Here we also see an effect of Rb: Simulations with larger Rb display larger two-particle vertical dispersions at late times. It is also worth pointing out that when the initial horizontal separation δr_0 is increased (for a given run), the short-time two-particle dispersion augments proportionally, but the late-time two-particle dispersion remains equal, indicating a decorrelation of the two particles at late times as reported before in Ref. [29] [note that in Fig. 16, as ζ_z^2 is normalized by δr_0^2, this late-time decorrelation results in different amplitudes of $(\zeta_z/\delta r_0)^2$ as δr_0^2 is changed].

As mentioned above, the two-particle vertical dispersion can be modeled using an extension of the single-particle model. As before, we consider the effect of the waves and of the turbulent eddies separately. First, if we have two particles which are initially very close to each other (almost at the same height, but with a horizontal displacement δr_0), we can assume they will be displaced by the same waves but with a phase difference between the two (for each wave with frequency ω) given by

$$\phi'_\omega \approx \phi_\omega + k\delta r_0. \tag{17}$$

Here ϕ_ω is the phase of the wave seen by one of the particles, ϕ'_ω is the phase seen by the other particle, k is the wave number, and we approximate the total separation between the two particles by δr_0 (as $\delta z_0 \ll \eta$). Using the expressions for the displacements of a particle in a superposition of random waves given by Eqs. (13) and (15), we can estimate the separation as a function of time for a single pair as

$$\zeta_{ij,(\mathrm{wav})}(t) = \sum_\omega A_\omega \{[\cos(\omega t + \phi_\omega) - \cos(\phi_\omega)] - [\cos(\omega t + \phi'_\omega) - \cos(\phi'_\omega)]\} + \delta z_0, \tag{18}$$

where the subindices i and j again label the pairs of particles that at the initial time meet the condition $\delta r_0 \approx \eta$ (or $\approx 2\eta$). Equation (18) is just the difference between two single-particle vertical trajectories, to which we added an initial vertical separation $\delta z_0 \ll \eta$. As we did in the preceding section, the resulting dispersion, when averaged over several pairs of particles and sets of random waves, can be approximated as (see Appendix B)

$$\left\langle \zeta^2_{z,(\mathrm{wav})} \right\rangle (t) \approx \begin{cases} U_z^2 \left(2.1 \delta r_0 \frac{2\pi}{L_\parallel}\right)^2 t^2 & \text{if } t < N^{-1} \\ Q_2(t) & \text{if } N^{-1} < t < 4N^{-1} \\ \frac{16 U_z^2 (2.1 \delta r_0 \pi)^2}{(L_\parallel N)^2} & \text{if } t \geqslant 4N^{-1}, \end{cases} \tag{19}$$

where, as in the single-particle approximation in Eq. (16), $Q_2(t)$ is a third-order polynomial interpolation for the two-particle case obtained by imposing the function and its derivative to be continuous in time and we neglected all terms in δz_0 and δz_0^2 as they are small when compared with the leading-order terms.

As at late times the particles separate significantly from each other, to take into account the effect of overturning we can assume that the two particles are uncorrelated and as a result we can just consider two independent CTRW processes with the same properties as the one described in the preceding section for single particles, one for each particle in the pair. This is compatible with observations of two-particle dispersion in DNSs of SST [29] and with the results from DNSs shown above, indicating that the late-time dispersion becomes independent of the original separation δr_0. The final result of combining $\zeta_{z,(\mathrm{wav})}$ with the CTRW processes is shown in Fig. 16. The model is in good agreement with the two-particle vertical dispersion obtained from the DNSs, both in the ballistic regime and for long times when dispersion becomes dominated by the turbulent eddies, for both forcing functions considered, different domain aspect ratios, and different values of Fr and Rb.

VII. CONCLUSION

In this paper we studied single- and two-particle vertical dispersion for Lagrangian trajectories in forced stably stratified turbulence, using two different forcing functions (Taylor-Green and random forcing), domains with different aspect ratios, and different Froude and Reynolds numbers. Using direct numerical simulations, we showed that late-time saturation of single-particle vertical dispersion, reported in previous studies of this problem, is obtained only for moderate values of the buoyancy Reynolds number and that for larger values of Rb, or even for moderate Rb in the case of the Taylor-Green flow that develops a vertical circulation, the saturation does not take place. Instead, δz^2 keeps growing in time after the ballistic regime, albeit at a slower rate than in homogeneous and isotropic turbulence.

We showed that the gradient Richardson number plays an important role in the strength of the vertical transport of Lagrangian tracers, as overturning fluid elements with $\mathrm{Ri}_g < 0$ give an important contribution to vertical displacement of Lagrangian particles. In particular, regions of the flows with higher vertical velocity present a higher probability of having particles with $\mathrm{Ri}_g < 0$ and vice versa. The joint probability (or restricted PDFs) between Ri_g and the Lagrangian vertical velocity, temperature fluctuations, and gradients were studied, confirming this correlation.

Based on these results, we derived models for single- and two-particle vertical dispersion that consist of a superposition of random waves (to capture the early-time ballistic regime) and an eddy-constrained continuous-time random-walk process (to capture the effect of turbulent eddies and overturning instabilities in the flow at late times). These models, together with the model for single-particle horizontal dispersion in Ref. [11], provide a description for the anisotropic dispersion in both the vertical and horizontal directions of stably stratified turbulence. The vertical dispersion obtained from the model presented here is in good agreement with the vertical dispersions obtained from the direct numerical simulations. This agreement strengthens the observation that the waves dominate the dynamic of particles at short times, resulting in the initial ballistic regime, while at intermediate times ($t \approx 2\pi/N$) linear and nonlinear effects coexist in the dynamics, giving rise to a transient that can develop (or not) a plateau on the dispersion depending on how strong (or weak) the effect of overturning events is. At later times, and if turbulence is sufficiently strong [as measured by Rb or, equivalently, by the probability of a fluid element to suffer overturning, $R = P(\mathrm{Ri}_g < 0)$], turbulence (modeled here by the continuous-time random-walk process) dominates. The superposition of linear and turbulent contributions to the dispersion in the model thus allows clarification of the relevant time and length scales involved in the dynamics of Lagrangian tracers in stratified turbulence. Finally, as all parameters in the model can be obtained from large-scale Eulerian properties of the flow, the model creates an opportunity for modeling turbulent dispersion of tracers in Eulerian simulations of stratified flows that do not resolve the smallest scales in the flow, as usually is the case in the study of atmospheric and oceanic flows.

ACKNOWLEDGMENT

The authors acknowledge support from PICT Grant No. 2015-3530.

APPENDIX A: DERIVATION OF THE SINGLE-PARTICLE DISPERSION WAVE MODEL

We want to derive averaged expressions for the dispersion as a function of time resulting from a random superposition of waves like that given by Eq. (15). For short times, from

$$\delta z_{\mathrm{wav}}(t) = \sum_{\omega} A_w[\cos(\omega t + \phi_\omega) - \cos(\phi_\omega)], \tag{A1}$$

we can take the square and use the trigonometric identity $\cos(\omega t + \phi_\omega) = \cos(\omega t)\cos(\phi_\omega) - \sin(\omega t)\sin(\phi_\omega)$, the Taylor expansions to first order $\sin(\omega t) \approx \omega t$ and $\cos(\omega t) \approx 1$, and Eq. (14)

with $A_0 = (2U_z^2/N_\omega)^{1/2}$ to get

$$\delta z^2_{\rm wav} \approx t^2 \frac{2U_z^2}{N_\omega}\left(\sum_\omega \sin(\phi_\omega)\right)\left(\sum_{\omega'} \sin(\phi_{\omega'})\right) = t^2\frac{2U_z^2}{N_\omega}\left(\sum_\omega \sin^2(\phi_\omega) + \sum_{\omega,\omega'\neq\omega} \sin(\phi_\omega)\sin(\phi_{\omega'})\right). \tag{A2}$$

As the average over random phases ϕ uniformly distributed between 0 and 2π is

$$\langle \sin(\phi)\rangle_\phi = \langle \cos(\phi)\rangle_\phi = 0, \tag{A3}$$

$$\langle \sin^2(\phi)\rangle_\phi = \langle \cos^2(\phi)\rangle_\phi = 1/2 \tag{A4}$$

for ϕ_ω and $\phi_{\omega'}$ two independent stochastic variables, for short times and after averaging over an ensemble of particles with different sets of random waves, we then have

$$\left\langle \delta z^2_{\rm wav}\right\rangle(t) \approx t^2 U_z^2. \tag{A5}$$

For long times

$$\delta z^2_{\rm wav}(t) = \frac{2U_z^2}{N_\omega}\left(\sum_\omega \frac{1}{\omega}[\cos(\omega t+\phi_\omega)-\cos(\phi_\omega)]\right)\left(\sum_{\omega'} \frac{1}{\omega'}[\cos(\omega' t+\phi_{\omega'})-\cos(\phi_{\omega'})]\right), \tag{A6}$$

which can be rewritten as

$$\delta z^2_{\rm wav}(t) = \frac{2U_z^2}{N_\omega}\left(\sum_\omega \frac{1}{\omega^2}[\cos(\omega t+\phi_\omega)-\cos(\phi_\omega)]^2 + \sum_{\omega,\omega'\neq\omega} \frac{1}{\omega\omega'}[\cos(\omega' t+\phi_{\omega'})-\cos(\phi_{\omega'})][\cos(\omega t+\phi_\omega)-\cos(\phi_\omega)]\right). \tag{A7}$$

As the time average over several wave periods results in $\langle\cos(\omega t+\phi_\omega)^2\rangle_t = 1/2$, $\langle\cos(\omega t+\phi_\omega)\rangle_t = 0$, and $\langle\cos(\omega t+\phi_\omega)\cos(\omega' t+\phi_{\omega'})\rangle_t = 0$, using Eqs. (A3) and (A4), we obtain the average of Eq. (A7) over time and over an ensemble of particles and random waves as

$$\left\langle \delta z^2_{\rm wav}\right\rangle_t \approx \frac{2U_z^2}{N_\omega}\sum_{\omega=\omega_{\rm min}}^{N}\frac{1}{\omega^2}. \tag{A8}$$

Using $\Delta\omega = (N-\omega_{\rm min})/N_\omega$, then

$$\sum_{\omega=\omega_{\rm min}}^{N}\frac{1}{\omega^2} = \sum_{\omega=\omega_{\rm min}}^{N}\frac{1}{\omega^2}\frac{\Delta\omega}{\Delta\omega} \approx \frac{1}{\Delta\omega}\int_{\omega_{\rm min}}^{N}\frac{1}{\omega^2}d\omega = \frac{1}{\Delta\omega}\frac{N-\omega_{\rm min}}{N\omega_{\rm min}} = \frac{N_\omega}{N\omega_{\rm min}} \tag{A9}$$

and finally Eq. (A8) can we rewritten as

$$\left\langle \delta z^2_{\rm wav}\right\rangle_t \approx \frac{2U_z^2}{N\omega_{\rm min}}, \tag{A10}$$

where we chose $\omega_{\rm min} = N/2$.

This gives the early-time ($t \leqslant N^{-1}$) and late-time ($t \geqslant 4N^{-1}$) expressions in Eq. (16) (note that the choices of N^{-1} and $4N^{-1}$ as the two limits for the validity of the approximations are somewhat arbitrary). To obtain a smooth [i.e., continuous in $\langle\delta z^2_{\rm wav}\rangle(t)$ and in its time derivative] interpolation between these two expressions, we use a third-order polynomial function to interpolate $\langle\delta z^2_{\rm wav}\rangle(t)$

between $t_a = 1/N$ and $t_b = 4/N$. Writing a polynomial approximation $\langle \delta z^2_{\rm wav}\rangle(t) = Q(t) = At^3 + Bt^2 + Ct + D$, then the coefficients after imposing the continuity conditions are

$$A = \{Q'(t_a)(t_a - t_b) - 2[Q(t_a) - Q(t_b)]\}/(t_a - t_b)^3, \tag{A11}$$

$$B = -\left\{Q'(t_a)\left(t_a^2 + t_a t_b - 2t_b^2\right) + 3(t_a + t_b)[Q(t_b) - Q(t_a)]\right\}/(t_a - t_b)^3, \tag{A12}$$

$$C = t_b\left\{Q'(t_a)\left(2t_a^2 - t_a t_b - t_b^2\right) + 6t_a[Q(t_b) - Q(t_a)]\right\}/(t_a - t_b)^3, \tag{A13}$$

$$D = -\left[t_a t_b^2 Q'(t_a)(t_a - t_b) + t_b^2 Q(t_a)(t_b - 3t_a) + t_a^2 Q(t_b) + (3t_b - t_a)\right]/(t_a - t_b)^3, \tag{A14}$$

where the values $Q(t_a)$ and $Q(t_b)$ are given by the expressions in Eqs. (16) and (19) evaluated at $t = N^{-1}$ or $t = 4N^{-1}$.

APPENDIX B: TWO-PARTICLE DISPERSION WAVE MODEL

To derive averaged expressions for the two-particle dispersion resulting from a random superposition of waves, we start from Eq. (18),

$$\begin{aligned}\zeta_{ij,(\rm wav)}(t) &= z_{i,(\rm wav)}(t) - z_{j,(\rm wav)}(t)\\ &= \sum_\omega A_\omega\{[\cos(\omega t + \phi_\omega) - \cos(\phi_\omega)] - [\cos(\omega t + \phi'_\omega) - \cos(\phi'_\omega)]\} + \delta z_0,\end{aligned} \tag{B1}$$

where ϕ'_ω is the phase of the wave with frequency ω as seen by the particle j, which is displaced a distance approximately equal to δr_0 (as $\delta z_0 \ll \delta r_0$) from the particle i (with phase ϕ_ω). Thus $\phi'_\omega \approx \phi_\omega + k\,\delta r_0$ (note that we ignore any increase in time of the horizontal distance between the two particles and in the following we consider only the increase in the vertical distance between them). We can approximate $k \approx K_\parallel/\cos\alpha$, where α is the angle of propagation of the waves with respect to the vertical direction and $K_\parallel$ is the parallel integral wave number as introduced in Sec. II. From the dispersion relation of internal gravity waves we have $\omega = N\sin\alpha$ (or $\sin\alpha = \omega/N$), and using $\cos\alpha = (1 - \sin^2\alpha)^{1/2}$ and that ω/N in the single-particle model is a random variable uniformly distributed between $1/2$ and 1, we can estimate the mean value of the wave number k for an ensemble of waves propagating in all available directions as

$$\langle k\rangle = \left\langle \frac{K_\parallel}{\cos\alpha}\right\rangle_{\omega/N} = 2K_\parallel \int_{1/2}^{1} \frac{d(\omega/N)}{\sqrt{1 - (\omega/N)^2}} \approx 2.1K_\parallel, \tag{B2}$$

where the factor 2 multiplying the integral comes from computing the mean of ω/N in the interval $[1/2, 1]$. Thus, the mean phase shift results to be $\langle\delta\phi\rangle \approx 2.1K_\parallel\delta r_0$.

The two-particle mean-square vertical displacement caused by the waves $\langle\zeta^2_{z,(\rm wav)}\rangle$ is the average over an ensemble of particle pairs of the square of the vertical two-particle displacements for a single pair $\zeta_{ij,(\rm wav)}$. For a very small initial separation between the particle pairs $\delta\phi$ is also small and we can use in Eq. (B1) the approximation $\cos(\omega t + \phi + \delta\phi) \approx \cos(\omega t + \phi) - \delta\phi\sin(\omega t + \phi)$ to get

$$\zeta_{ij,(\rm wav)} \approx \sum_\omega -k\delta r_0 A_\omega[\sin(\omega t + \phi_\omega) - \sin(\phi_\omega)] + \delta z_0. \tag{B3}$$

For short times we can take the first-order Taylor approximations $\sin(\omega t) \approx -\omega t$ and $\cos(\omega t) \approx 1$. Also, using the trigonometrical identity $\sin(\omega t + \phi_\omega) = \sin(\omega t)\cos(\phi_\omega) + \cos(\omega t)\sin(\phi_\omega)$, we obtain

$$\zeta_{ij,(\rm wav)} \approx t\delta r_0 \sum_\omega[-\omega k A_\omega\cos(\phi_\omega)] + \delta z_0. \tag{B4}$$

Finally, we take the ensemble average of the square of $\zeta_{ij,(\mathrm{wav})}$, we use that α and ω are stochastic variables, we use Eq. (14) for A_ω, and we use Eqs. (B2), (A3), and (A4) to get

$$\langle \zeta^2_{\mathrm{wav}} \rangle(t) \approx U_z^2 (2.1 K_\parallel \delta r_0)^2 t^2, \tag{B5}$$

where terms in δz_0 and δz_0^2 are neglected for being much smaller than the leading-order term.

To obtain the long-time approximation we start by neglecting the term δz_0 and taking the mean-square value of Eq. (B1),

$$\begin{aligned}\langle \zeta^2_{ij,(\mathrm{wav})} \rangle = \Bigg\langle \sum_\omega A_\omega^2 \{ &[\cos(\omega t + \phi_\omega) - \cos(\phi_\omega)]^2 + [\cos(\omega t + \phi'_\omega) - \cos(\phi'_\omega)]^2 \\ &- 2[\cos(\omega t + \phi_\omega) - \cos(\phi_\omega)][\cos(\omega t + \phi'_\omega) - \cos(\phi'_\omega)]\} + \sum_{\omega,\omega' \neq \omega} (\cdots) \Bigg\rangle,\end{aligned} \tag{B6}$$

where the mean is taken both over time and over particle pairs. The cross-product terms in Eq. (B6) have mean value $\langle \sum_{\omega,\omega' \neq \omega} (\cdots) \rangle = 0$, as discussed in Appendix A. Using again the approximation $\cos(\omega t + \phi_\omega + \delta\phi) \approx \cos(\omega t + \phi_\omega) - \delta\phi \sin(\omega t + \phi)$, we get

$$\begin{aligned}\langle \zeta^2_{ij,(\mathrm{wav})} \rangle \approx \Bigg\langle \sum_\omega A_\omega^2 \{ &[\cos(\omega t + \phi_\omega) - \cos(\phi_\omega)]^2 + [\cos(\omega t + \phi_\omega) - \cos(\phi_\omega) \\ &- \delta\phi(\sin(\omega t + \phi_\omega) - \sin(\phi))]^2 - 2[\cos(\omega t + \phi_\omega) - \cos(\phi_\omega)] \\ &\times [\cos(\omega t + \phi_\omega) - \cos(\phi_\omega) - \delta\phi(\sin(\omega t + \phi_\omega) - \sin(\phi))]\} \Bigg\rangle.\end{aligned} \tag{B7}$$

Finally, using Eqs. (A3), (A4), (A7), (A8), and (A10) and given that $\langle \sin(\phi)\cos(\phi) \rangle_\phi = 0$ with ϕ uniformly distributed between 0 and 2π, we have

$$\langle \zeta^2_{z,(\mathrm{wav})} \rangle_t \approx \langle (k\delta r_0)^2 \rangle \left\langle \sum_\omega A_\omega^2 [\sin(\omega t + \phi) - \sin(\phi)] \right\rangle_t \approx \langle (k\delta r_0)^2 \rangle \langle \delta z^2_{\mathrm{wav}} \rangle_t \approx \frac{2(2.1 K_\parallel \delta r_0)^2 U_z^2}{N \omega_{\min}}. \tag{B8}$$

[1] J. C. Wyngaard, Atmospheric turbulence, Annu. Rev. Fluid Mech. **24**, 205 (1992).

[2] E. A. D'Asaro and R.-C. Lien, Lagrangian measurements of waves and turbulence in stratified flows, J. Phys. Oceanogr. **30**, 641 (2000).

[3] T. Watanabe, J. J. Riley, and K. Nagata, Turbulent entrainment across turbulent-nonturbulent interfaces in stably stratified mixing layers, Phys. Rev. Fluids **2**, 104803 (2017).

[4] G. Amir, N. Bar, A. Eidelman, T. Elperin, N. Kleeorin, and I. Rogachevskii, Turbulent thermal diffusion in strongly stratified turbulence: Theory and experiments, Phys. Rev. Fluids **2**, 064605 (2017).

[5] E. Lindborg and G. Brethouwer, Vertical dispersion by stratified turbulence, J. Fluid Mech. **614**, 303 (2008).

[6] M. L. Waite, Stratified turbulence at the buoyancy scale, Phys. Fluids **23**, 066602 (2011).

[7] R. Marino, P. D. Mininni, D. L. Rosenberg, and A. Pouquet, Large-scale anisotropy in stably stratified rotating flows, Phys. Rev. E **90**, 023018 (2014).

[8] A. Maffioli, Vertical spectra of stratified turbulence at large horizontal scales, Phys. Rev. Fluids **2**, 104802 (2017).

[9] L. M. Smith and F. Waleffe, Generation of slow large scales in forced rotating stratified turbulence, J. Fluid Mech. **451**, 145 (2002).

[10] P. Clark di Leoni and P. D. Mininni, Absorption of waves by large-scale winds in stratified turbulence, Phys. Rev. E **91**, 033015 (2015).
[11] N. E. Sujovolsky, P. D. Mininni, and M. P. Rast, Single-particle dispersion in stably stratified turbulence, Phys. Rev. Fluids **3**, 034603 (2018).
[12] Y. Kimura and J. R. Herring, Diffusion in stably stratified turbulence, J. Fluid Mech. **328**, 253 (1996).
[13] Y. Kaneda and T. Ishida, Suppression of vertical diffusion in strongly stratified turbulence, J. Fluid Mech. **402**, 311 (2000).
[14] L. Liechtenstein, F. S. Godeferd, and C. Cambon, The role of nonlinearity in turbulent diffusion models for stably stratified and rotating turbulence, Int. J. Heat Fluid Fl. **27**, 644 (2006).
[15] C. Rorai, P. D. Mininni, and A. Pouquet, Turbulence comes in bursts in stably stratified flows, Phys. Rev. E **89**, 043002 (2014).
[16] F. Feraco, R. Marino, A. Pumir, L. Primavera, P. D. Mininni, A. Pouquet, and D. Rosenberg, Vertical drafts and mixing in stratified turbulence: Sharp transition with Froude number, Europhys. Lett. **123**, 44002 (2018).
[17] P. Billant and J.-M. Chomaz, Self-similarity of strongly stratified inviscid flows, Phys. Fluids **13**, 1645 (2001).
[18] S. M. de Bruyn Kops, J. J. Riley, and K. B. Winters, Reynolds and Froude number scaling in stably-stratified flows, in *IUTAM Symposium on Reynolds Number Scaling in Turbulent Flow* (Springer, Dordrecht, 2004), Vol. 74, pp. 71–76.
[19] E. Bauer, Dispersion of tracers in the atmosphere and ocean: Survey and comparison of experimental data, J. Geophys. Res. **79**, 789 (1974).
[20] H. J. S. Fernando, Turbulent mixing in stratified fluids, Annu. Rev. Fluid Mech. **23**, 455 (1991).
[21] K. L. Polzin, J. M. Toole, J. R. Ledwell, and R. W. Schmitt, Spatial variability of turbulent mixing in the abyssal ocean, Science **276**, 93 (1997).
[22] C. Wunsch and R. Ferrari, Vertical mixing, energy, and the general circulation of the oceans, Annu. Rev. Fluid Mech. **36**, 281 (2004).
[23] G. N. Ivey, K. B. Winters, and J. R. Koseff, Density stratification, turbulence, but how much mixing? Annu. Rev. Fluid Mech. **40**, 169 (2008).
[24] P. Klein and G. Lapeyre, The oceanic vertical pump induced by mesoscale and submesoscale turbulence, Annu. Rev. Mar. Sci. **1**, 351 (2009).
[25] L. A. Mingari, E. A. Collini, A. Folch, W. Báez, E. Bustos, M. S. Osores, F. Reckziegel, P. Alexander, and J. G. Viramonte, Numerical simulations of windblown dust over complex terrain: The Fiambalá Basin episode in June 2015, Atmos. Chem. Phys. **17**, 6759 (2017).
[26] A. Jones, D. Thomson, M. Hort, and B. Devenish, in *Air Pollution Modeling and its Application XVII*, edited by C. Borrego and A. L. Norman (Springer, Boston, 2007), pp. 580–589.
[27] F. S. Godeferd, N. A. Malik, C. Cambon, and F. Nicolleau, Eulerian and Lagrangian statistics in homogeneous stratified flows, Appl. Sci. Res. **57**, 319 (1996).
[28] F. Nicolleau and J. C. Vassilicos, Turbulent diffusion in stably stratified non-decaying turbulence, J. Fluid Mech. **410**, 123 (2000).
[29] M. van Aartrijk, H. J. H. Clercx, and K. B. Winters, Single-particle, particle-pair, and multiparticle dispersion of fluid particles in forced stably stratified turbulence, Phys. Fluids **20**, 025104 (2008).
[30] J. Bec, L. Biferale, M. Cencini, A. Lanotte, S. Musacchio, and F. Toschi, Heavy Particle Concentration in Turbulence at Dissipative and Inertial Scales, Phys. Rev. Lett. **98**, 084502 (2007).
[31] S. Sumbekova, A. Cartellier, A. Aliseda, and M. Bourgoin, Preferential concentration of inertial sub-Kolmogorov particles: The roles of mass loading of particles, Stokes numbers, and Reynolds numbers, Phys. Rev. Fluids **2**, 024302 (2017).
[32] M. van Aartrijk and H. J. H. Clercx, Vertical dispersion of light inertial particles in stably stratified turbulence: The influence of the Basset force, Phys. Fluids **22**, 013301 (2010).
[33] A. Sozza, F. De Lillo, S. Musacchio, and G. Boffetta, Large-scale confinement and small-scale clustering of floating particles in stratified turbulence, Phys. Rev. Fluids **1**, 052401(R) (2016).
[34] A. Sozza, F. De Lillo, and G. Boffetta, Inertial floaters in stratified turbulence, Europhys. Lett. **121**, 14002 (2018).

[35] P. D. Mininni, D. Rosenberg, R. Reddy, and A. Pouquet, A hybrid MPI-OpenMP scheme for scalable parallel pseudospectral computations for fluid turbulence, Parallel Comput. **37**, 316 (2011).
[36] P. K. Yeung and S. B. Pope, An algorithm for tracking fluid particles in numerical simulations of homogeneous turbulence, J. Comput. Phys. **79**, 373 (1988).
[37] N. E. Sujovolsky, P. D. Mininni, and A. Pouquet, Generation of turbulence through frontogenesis in sheared stratified flows, Phys. Fluids **30**, 086601 (2018).
[38] P. Billant and J.-M. Chomaz, Theoretical analysis of the zigzag instability of a vertical columnar vortex pair in a strongly stratified fluid, J. Fluid Mech. **419**, 29 (2000).
[39] J. J. Riley and S. M. de Bruyn Kops, Dynamics of turbulence strongly influenced by buoyancy, Phys. Fluids **15**, 2047 (2003).
[40] P. A. Davidson, *Turbulence in Rotating, Stratified and Electrically Conducting Fluids* (Cambridge University Press, Cambridge, 2013).
[41] M. P. Rast, J.-F. Pinton, and P. D. Mininni, Turbulent transport with intermittency: Expectation of a scalar concentration, Phys. Rev. E **93**, 043120 (2016).